Supplemental Material for "Crystal Structure Prediction and Phase Stability in Highly Anharmonic Silver-Based Chalcohalide Antiperovskites"

Pol Benítez, Cibrán López, Josep-Lluís Tamarit, and Claudio Cazorla

Group of Characterization of Materials, Departament de Física, Universitat Politècnica de Catalunya, Campus Diagonal-Besòs, Av. Eduard Maristany 10–14, 08019 Barcelona, Spain and Research Center in Multiscale Science and Engineering, Universitat Politècnica de Catalunya, Campus Diagonal-Besòs, Av. Eduard Maristany 10–14, 08019 Barcelona, Spain

Cong Liu

Departament de Física, Universitat Politècnica de Catalunya, Campus Nord, Jordi Girona 1–3, 08005 Barcelona, Spain

Ivan Caño and Edgardo Saucedo

Research Center in Multiscale Science and Engineering, Universitat Politècnica de Catalunya, Campus Diagonal-Besòs, Av. Eduard Maristany 10–14, 08019 Barcelona, Spain and Department of Electronic Engineering, Universitat Politècnica de Catalunya, 08034 Barcelona, Spain

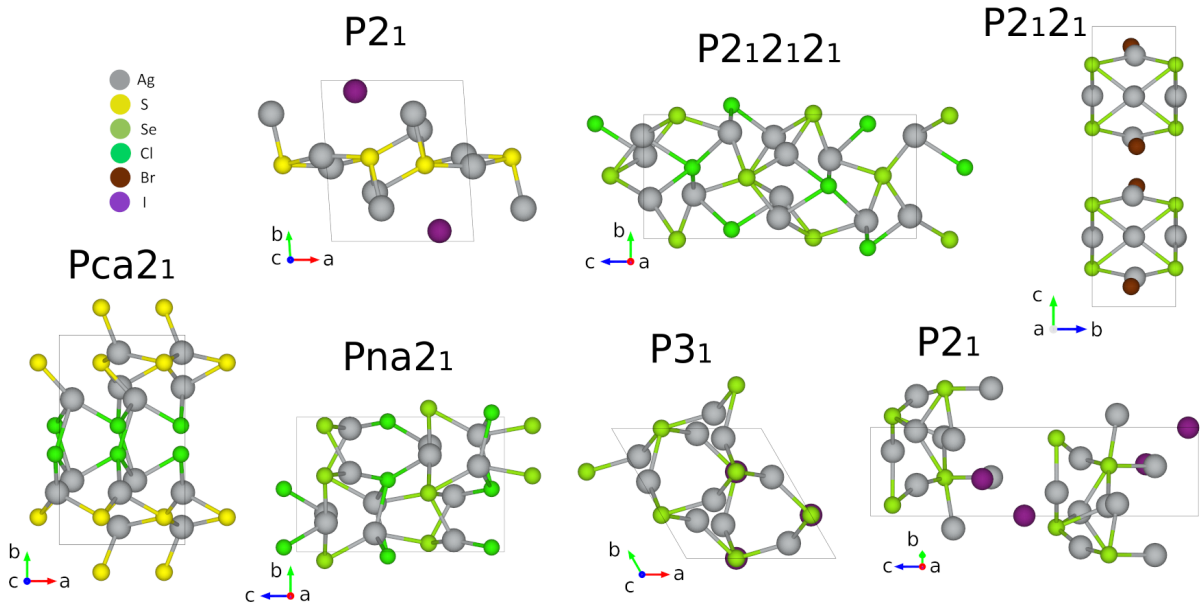

Supplemental Figure 1: Sketch of some energetically competitive crystal structures predicted with CSP-DFT methods for silver-based chalcohalide anti-perovskites.

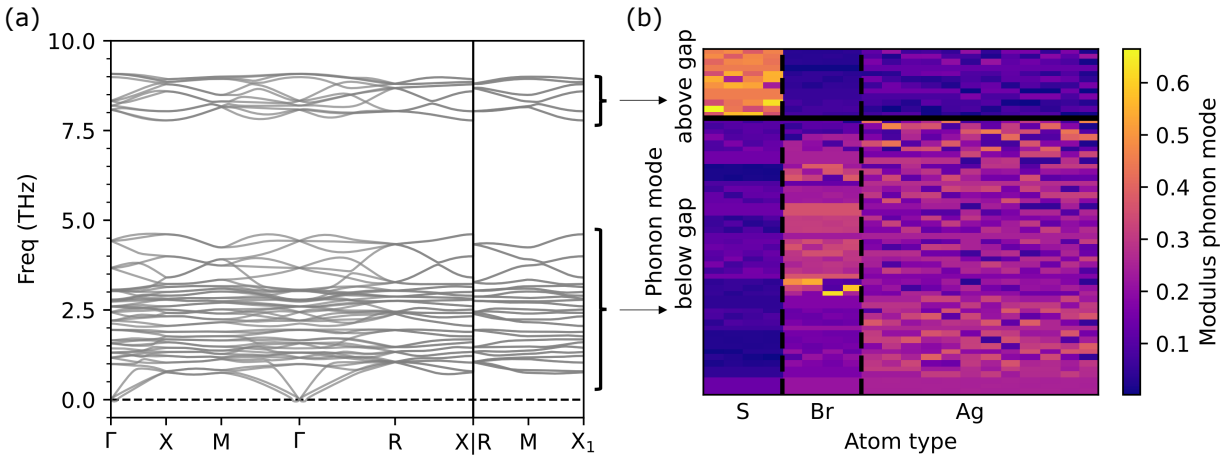

Supplemental Figure 2: Phonon analysis of the cubic $P2_13$ phase for Ag_3SBr. (a) Phonon dispersion exhibiting a phonon band gap. (b) Heat map showing the partial atomic contributions to the phonons calculated at Γ. The arrows between the two subplots group the results obtained above and below the phonon gap.

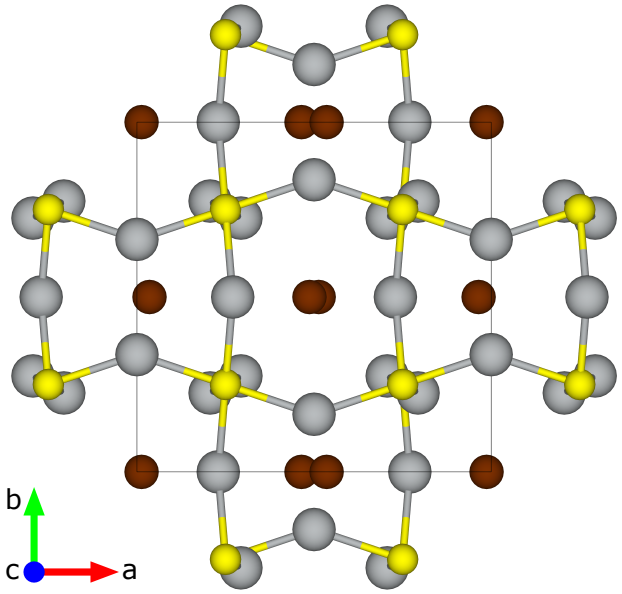

Supplemental Figure 3: Sketch of the orthorhombic *Cmcm* phase for Ag_3SBr.

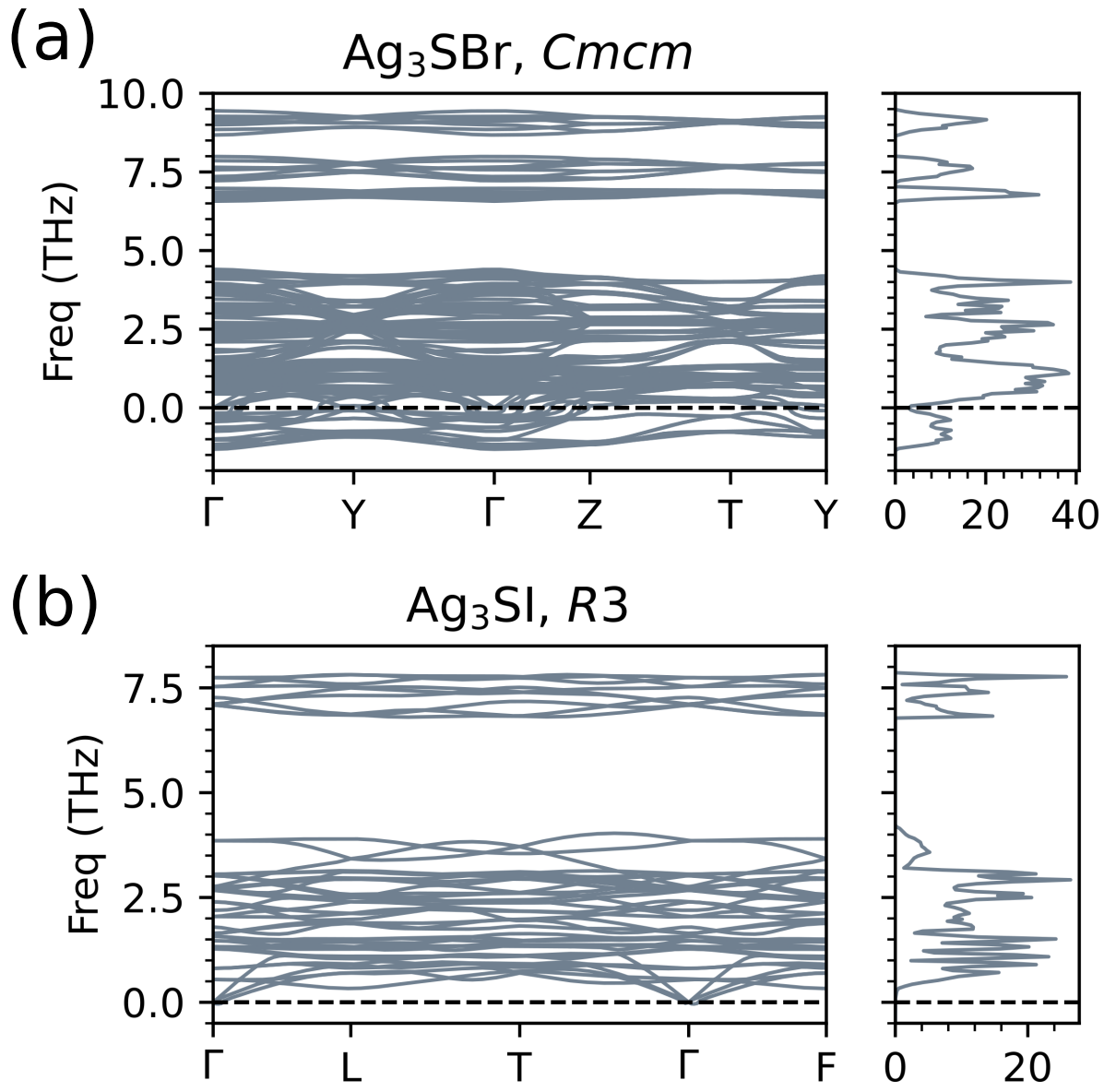

Supplemental Figure 4: Vibrational phonon spectrum of Ag_3SBr in the orthorhombic *Cmcm* phase and Ag_3SI in the trigonal *R*3 phase. Phonon calculations were performed at zero-temperature conditions. Results were obtained with the semi-local PBEsol functional.

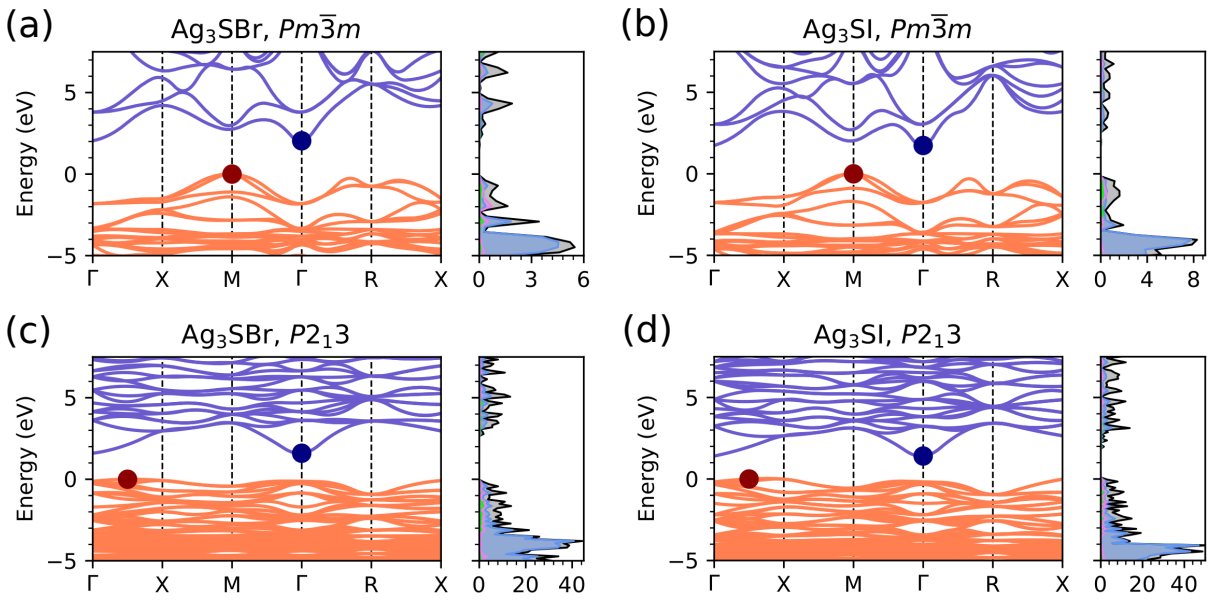

Supplemental Figure 5: Electronic band-structure properties of Ag_3SBr and Ag_3SI in their predicted ground state (cubic $P2_13$) and experimentally observed room-temperature phase (cubic $Pm\bar{3}m$). The calculations were performed at the HSE06+SOC level of theory, using a hybrid exchange-correlation energy functional and considering spin-orbit coupling effects. The big red (blue) dots indicate the top (bottom) of the valence (conduction) band. The density of electronic states is also represented for each system (right panels), where the grey, blue, green and pink curves refer to the total, Ag, S and Br/I cases.

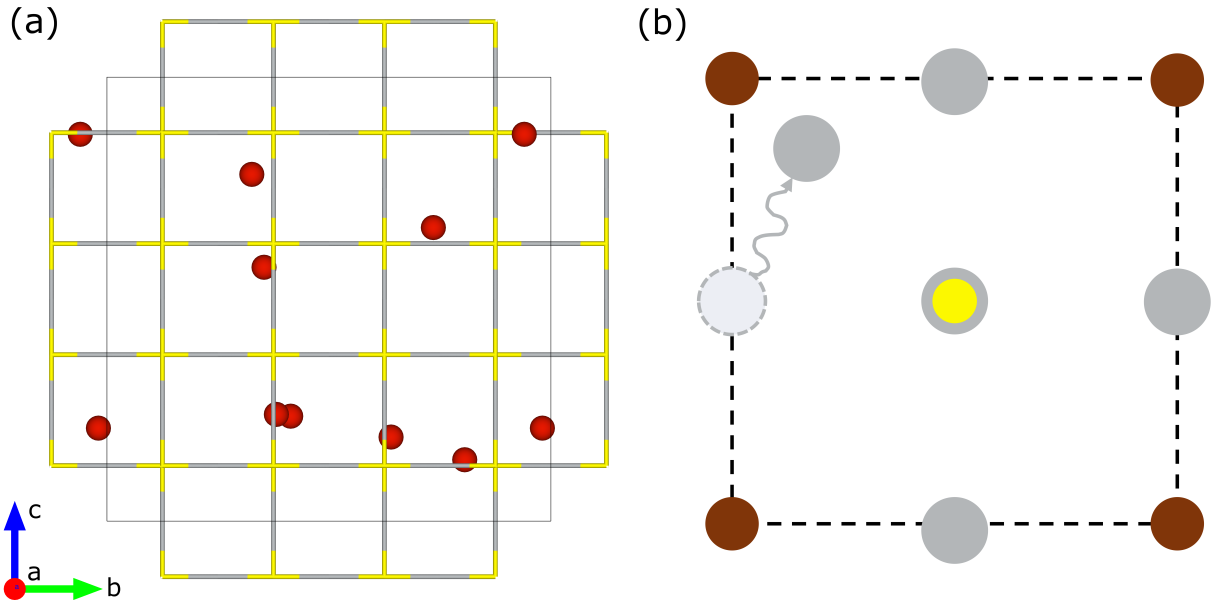

Supplemental Figure 6: (a) Silver interstitial positions mediating ionic diffusion, represented as red balls in the supercell, for Ag_3SBr at $T = 600$ K (cubic $Pm\bar{3}m$ phase). Vibrating Ag and S atoms are represented with sticks to enhance figure clarity (Br atoms are omitted for the same reason). (b) Diagram schematizing the Ag interstitial diffusion process. Ag, S, and Br atoms are represented with silver, yellow, and brown spheres, respectively. In average, mobile Ag ions spend approximately 6.9 ps in the identified interstitial positions.

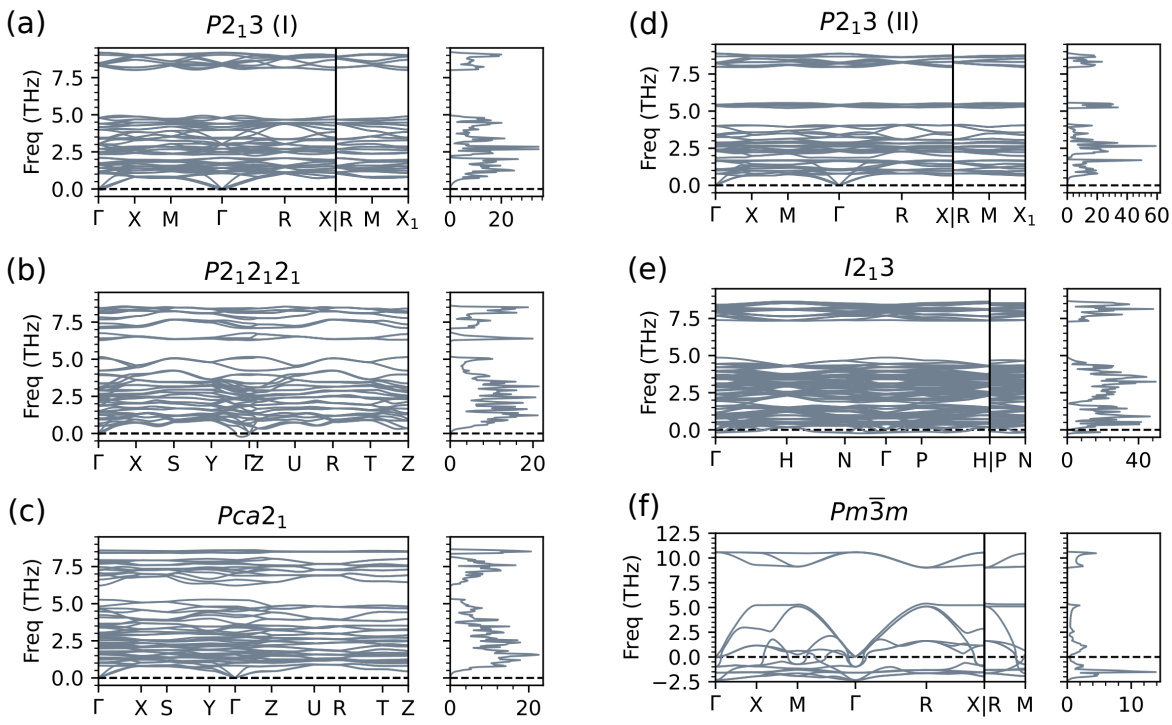

Supplemental Figure 7: Vibrational phonon spectrum of Ag_3SCl calculated for different crystal structures. Phonon calculations were performed at zero-temperature conditions. Results were obtained with the semi-local PBEsol functional.

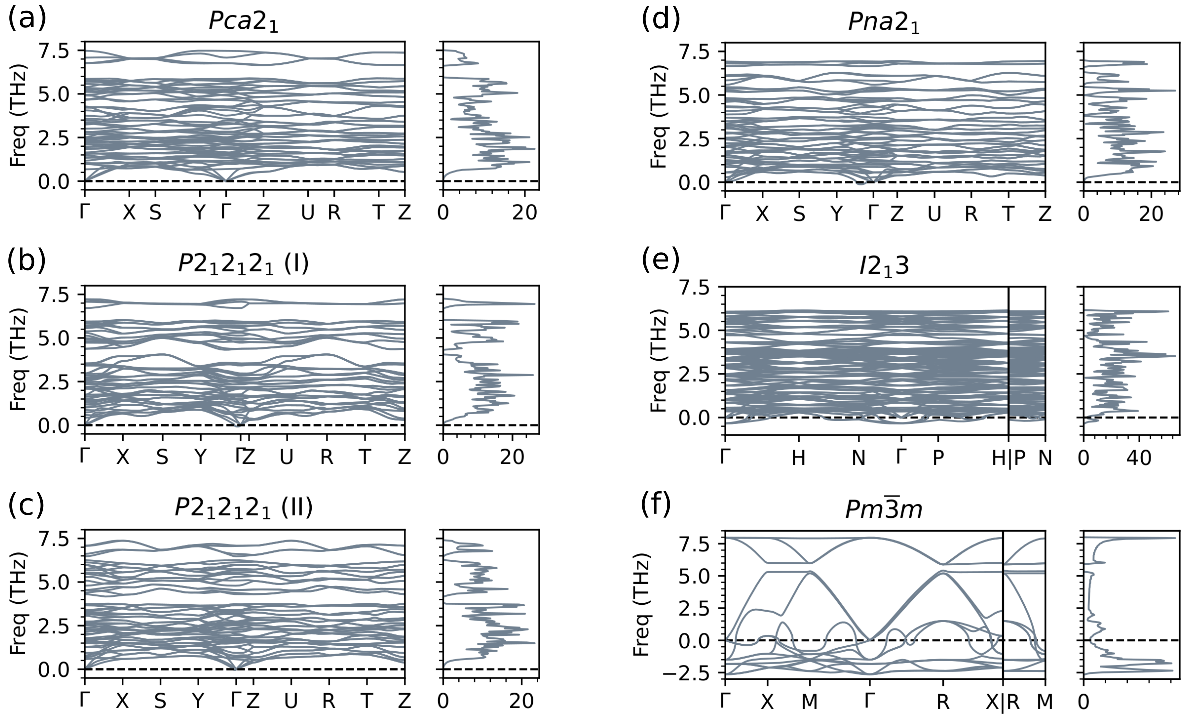

Supplemental Figure 8: Vibrational phonon spectrum of Ag_3SeCl calculated for different crystal structures. Phonon calculations were performed at zero-temperature conditions. Results were obtained with the semi-local PBEsol functional.

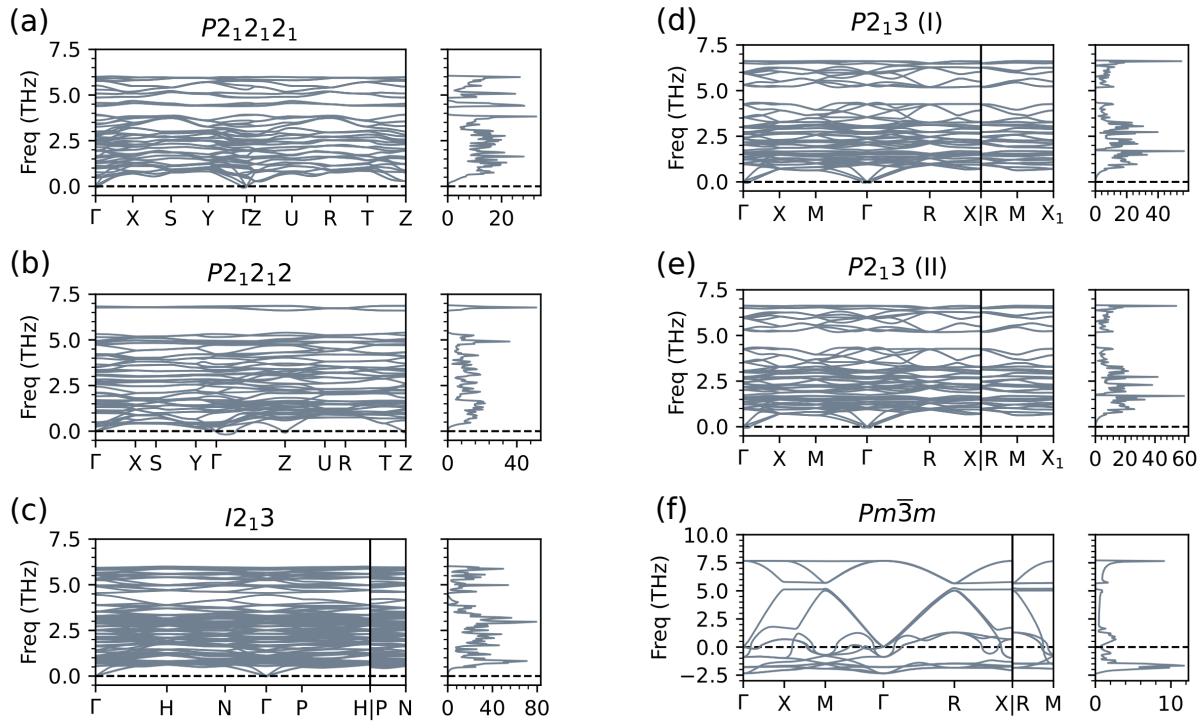

Supplemental Figure 9: Vibrational phonon spectrum of Ag_3SeBr calculated for different crystal structures. Phonon calculations were performed at zero-temperature conditions. Results were obtained with the semi-local PBEsol functional.

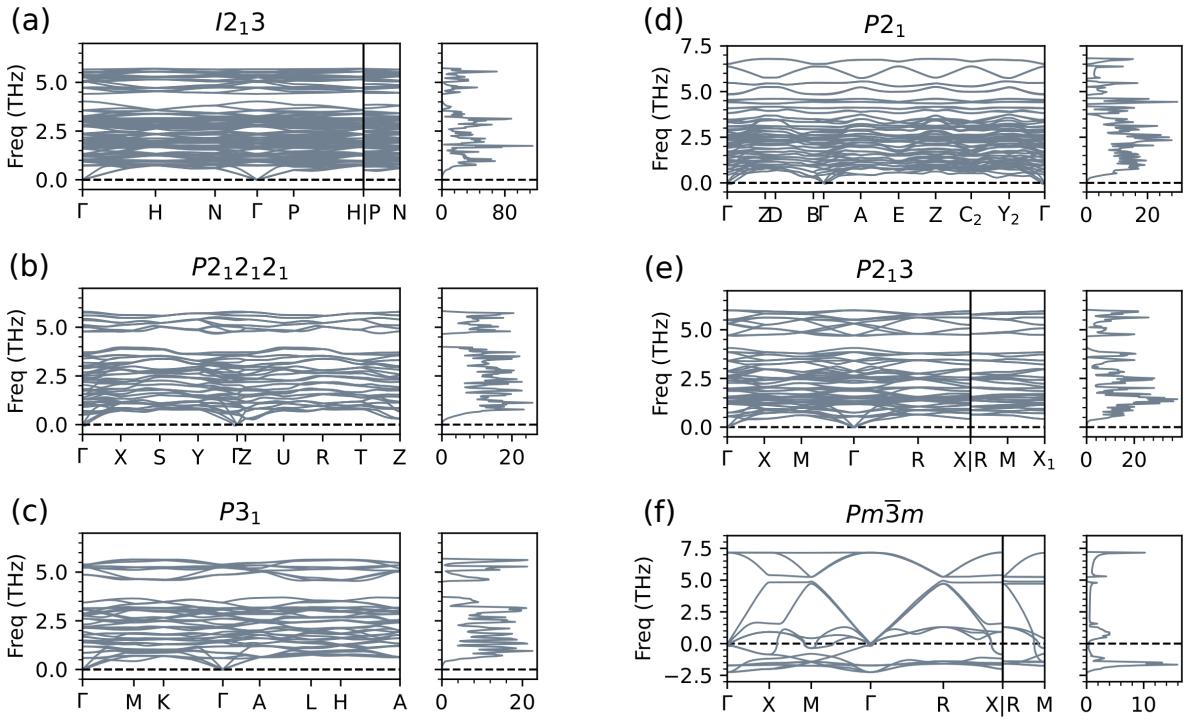

Supplemental Figure 10: Vibrational phonon spectrum of Ag_3SeI calculated for different crystal structures. Phonon calculations were performed at zero-temperature conditions. Results were obtained with the semi-local PBEsol functional.

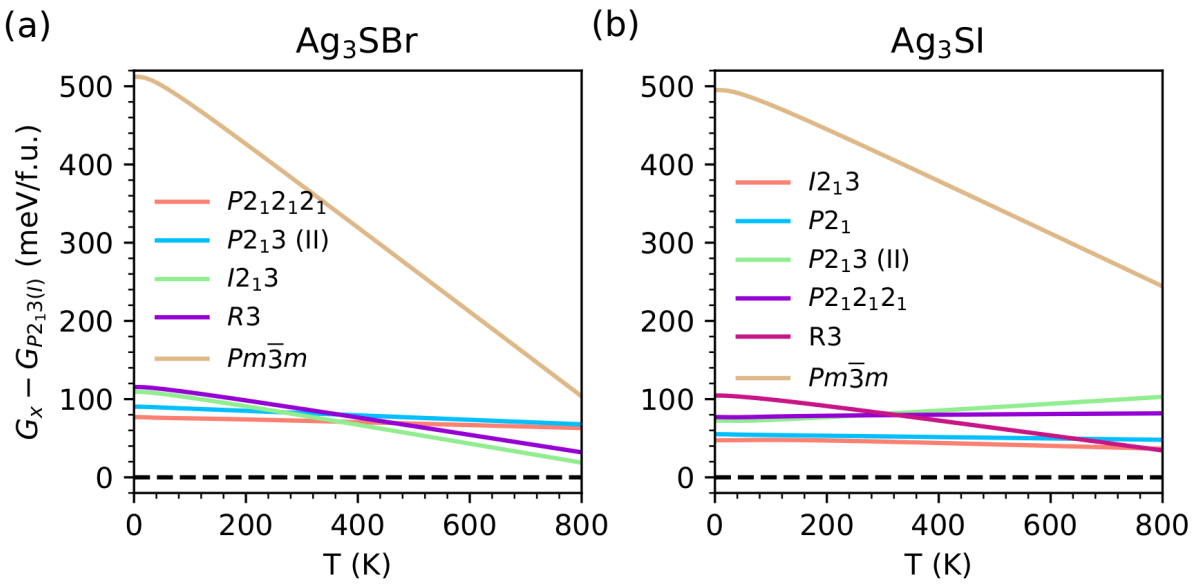

Supplemental Figure 11: CAP phase competition determined at $T \neq 0$ conditions. QH Helmholtz free-energy differences, ΔG, were calculated within the quasi-harmonic approximation and considering T-renormalized phonons for the cubic $Pm\bar{3}m$ phase. Results were obtained with the semi-local functional PBEsol.

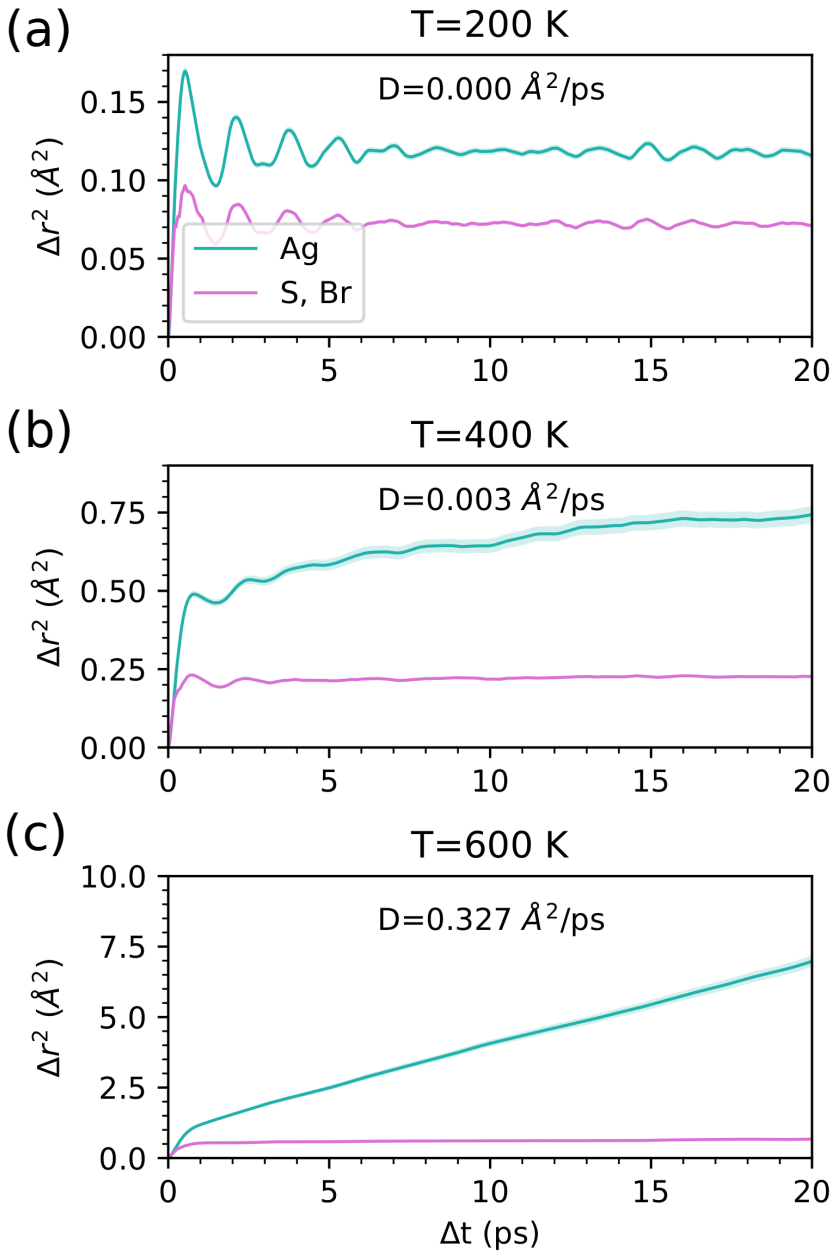

Supplemental Figure 12: Analysis of superionicity obtained from *ab initio* molecular dynamics simulations. Ag_3SBr in the cubic $P2_13$ phase at different temperatures. Results were obtained with the semi-local functional PBEsol.

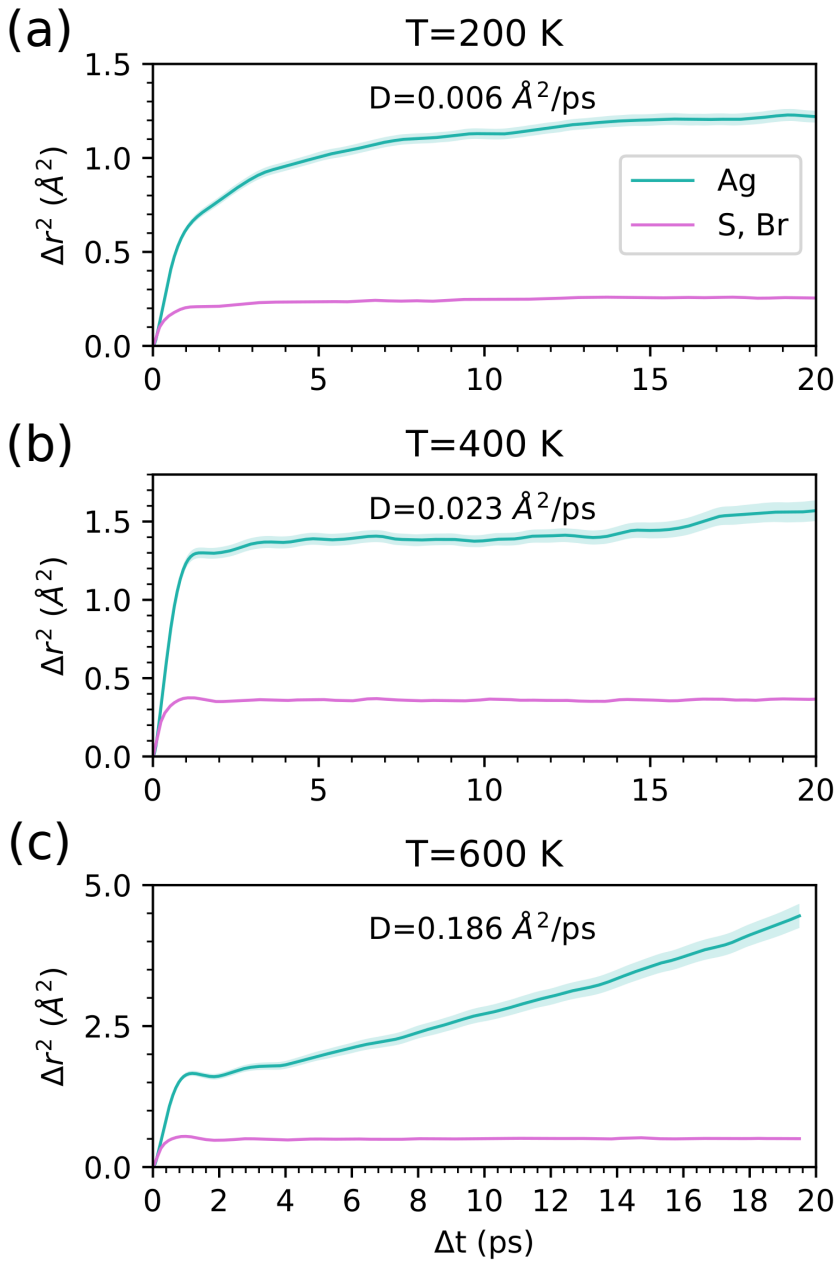

Supplemental Figure 13: Analysis of superionicity obtained from *ab initio* molecular dynamics simulations. Ag_3SBr in the cubic $Pm\bar{3}m$ phase at different temperatures. Results were obtained with the semi-local functional PBEsol.

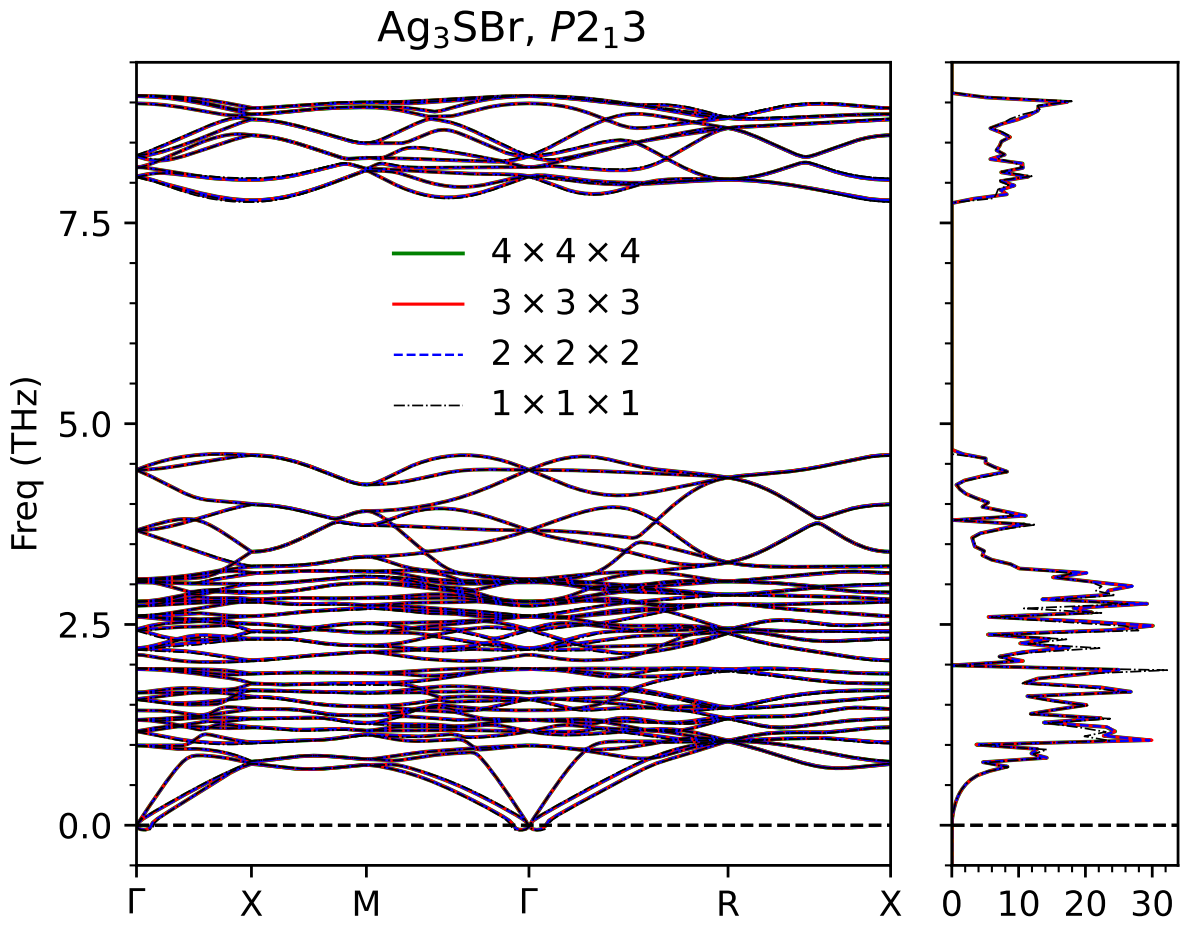

Supplemental Figure 14: Numerical test on the **k**-point grid employed for the calculation of full phonon spectra. The default **k**-point grid in our phonons calculations was of $3 \times 3 \times 3$. By either increasing or decreasing the density of the **k**-point grid, it is shown that the resulting phonon spectrum barely changes.

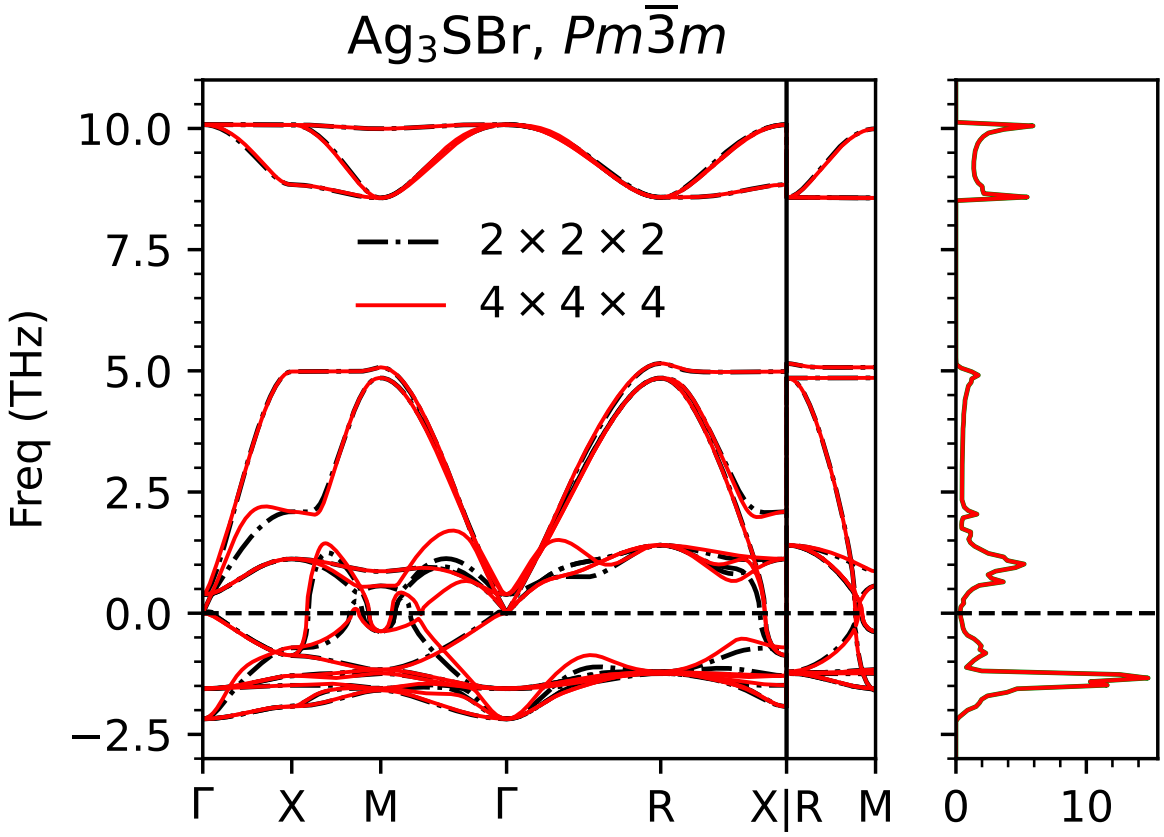

Supplemental Figure 15: Numerical test on the size of the supercell employed for the calculation of the full phonon spectra. By increasing the size of the supercell from $2 \times 2 \times 2$ to $4 \times 4 \times 4$, keeping the same **k**-point grid density, it is shown that likely size effects on the results obtained with the smaller supercell are not significant.

SUPPLEMENTAL DISCUSSION

Our zero-temperature phonon calculations for the cubic $Pm\bar{3}m$ phase were performed using the finite-differences method with large $4 \times 4 \times 4$ supercells containing 320 atoms and dense **k**-point grids of $2 \times 2 \times 2$ for reciprocal space sampling. Meanwhile, the temperature-renormalized phonon calculations were performed using a normal-mode-decomposition technique. This method, in addition to the calculated zero-temperature second-order interatomic force constants, requires the output of adequately equilibrated and computationally very intensive *ab initio* molecular dynamics (AIMD) simulations (see the "Methods" section in the main text).

To achieve numerical consistency and high accuracy in the temperature-renormalized phonon calculations, it is necessary to keep the same supercell size and **k**-point grid in both the zero-temperature second-order interatomic force constant estimations and AIMD simulations. However, performing AIMD simulations with large supercells (e.g., $4 \times 4 \times 4$) and dense **k**-point grids ($2 \times 2 \times 2$) is computationally prohibitive in practice, meaning that typically only single Γ-point reciprocal-space sampling is employed in the AIMD simulations.

To achieve numerical consistency and high accuracy in the temperature-renormalized phonon calculations of the cubic $Pm\bar{3}m$ phase, while simultaneously allowing for computational affordability, we reduced the size of the supercells to $2 \times 2 \times 2$ and used a **k**-point grid of $4 \times 4 \times 4$. The phonon spectrum results shown in Fig.12 of the main text were obtained using these technical parameters. Supplemental Fig.12 shows the phonon frequencies calculated at zero temperature by using a $4 \times 4 \times 4$ and a $2 \times 2 \times 2$ supercell, keeping the same **k**-point grid density. Therein, it is observed that likely size effects on the calculations performed with the smaller supercell are not significant at zero temperature. It seems reasonable then to assume a same behaviour at finite temperature conditions, thus validiting the results shown in Fig.12 of the main text.